

Article

Comparison of Aqua/Terra MODIS and Himawari-8 Satellite Data on Cloud Mask and Cloud Type Classification Using Split Window Algorithm

Babag Purbantoro ^{1,2,*}, Jamrud Aminuddin ³, Naohiro Manago ¹, Koichi Toyoshima ¹, Nofel Lagrosas ¹, Josaphat Tetuko Sri Sumantyo ¹ and Hiroaki Kuze ¹

¹ Center for Environmental Remote Sensing, Chiba University, Chiba 2638522, Japan; manago.naohiro@chiba-u.jp (N.M.); toyoshima@chiba-u.jp (K.T.); nofel@chiba-u.jp (N.L.); jtetukoss@faculty.chiba-u.jp (J.T.S.S.); hkuze@@faculty.chiba-u.jp (H.K.)

² Remote Sensing Technology and Data Center, Indonesian Institute of Aeronautics and Space (LAPAN), Jakarta 13710, Indonesia

³ Department of Physics, Faculty of Mathematics and Natural Science, Universitas Jenderal Soedirman, Central Java 53123, Indonesia; jamrud.aminuddin@unsoed.ac.id

* Correspondence: babag.purbantoro@lapan.go.id

Received: 5 October 2019; Accepted: 2 December 2019; Published: 9 December 2019



Abstract: Cloud classification is not only important for weather forecasts, but also for radiation budget studies. Although cloud mask and classification procedures have been proposed for Himawari-8 Advanced Himawari Imager (AHI), their applicability is still limited to daytime imagery. The split window algorithm (SWA), which is a mature algorithm that has long been exploited in the cloud analysis of satellite images, is based on the scatter diagram between the brightness temperature (BT) and BT difference (BTD). The purpose of this research is to examine the usefulness of the SWA for the cloud classification of both daytime and nighttime images from AHI. We apply SWA also to the image data from Moderate Resolution Imaging Spectroradiometer (MODIS) onboard Aqua and Terra to highlight the capability of AHI. We implement the cloud analysis around Japan by employing band 3 (0.469 μm) of MODIS and band 1 (0.47 μm) of AHI for extracting the cloud-covered regions in daytime. In the nighttime case, the bands that are centered at 3.9, 11, 12, and 13 μm are utilized for both MODIS and Himawari-8, with somewhat different combinations for land and sea areas. Thus, different thresholds are used for analyzing summer and winter images. Optimum values for BT and BTD thresholds are determined for the band pairs of band 31 (11.03 μm) and 32 (12.02 μm) of MODIS (SWA31-32) and band 13 (10.4 μm) and 15 (12.4 μm) of AHI (SWA13-15) in the implementation of SWA. The resulting cloud mask and classification are verified while using MODIS standard product (MYD35) and Cloud-Aerosol Lidar and Infrared Pathfinder Satellite Observation (CALIPSO) data. It is found that MODIS and AHI results both capture the essential characteristics of clouds reasonably well in spite of the relatively simple scheme of SWA based on four threshold values, although a broader spread of BTD obtained with Himawari-8 AHI (SWA13-15) could possibly lead to more consistent results for cloud-type classification than SWA31-32 based on the MODIS sensors.

Keywords: Himawari-8 AHI; Aqua MODIS; Terra MODIS; cloud mask; cloud type classification; split window algorithm; brightness temperature

1. Introduction

Cloud classification plays a crucial role in atmospheric and meteorology science. The amount and types of clouds both significantly influence the temperature of the Earth's surface, because of their capability to reflect and absorb solar radiation [1,2]. In recent decades, cloud characterization has

widely been conducted while using satellite data, especially from the Moderate Resolution Imaging Spectroradiometer (MODIS) sensor onboard Aqua [3,4] and Terra [5,6] satellites. Aqua has an ascending path that provides observations during 12.00–14.00 h local time in the daytime and 00.00–03.00 h in the nighttime. On the other hand, Terra has a descending path with observations at around 10.00–12.00 h in the daytime and 21.00–23.00 h in the nighttime. MODIS sensors onboard Aqua and Terra acquire image data at 36 different wavelength bands, which cover visible (20 bands) and infrared (16 bands) spectral ranges with spatial resolutions of 250, 500, and 1000 m [7]. Such availability of multi-spectral information is the key advantage of MODIS data for detailed analysis of the atmosphere and Earth's surfaces. Ackerman et al. [5] and Frey et al. [8] report the MODIS product related to the cloud mask. Other related studies include the nighttime cloud detection by Ackerman et al. [5], cloud phase by Strabala et al. [9], snow cover by Hall et al. [10], and classification mask by Li et al. [3].

The Advanced Himawari Imager (AHI) sensor onboard the Himawari-8 meteorological satellite has made carrying out the high-frequency observation of clouds possible. The acquisition interval is 2.5 min. for the Japan area and 10 min. for the full disk [11]. This is advantageous for the high-temporal characterization of clouds. The AHI sensor has 16 bands, which include three visible bands, three near-infrared (NIR) bands, and ten thermal infrared (TIR) bands with spatial resolutions of 0.5–2 km [11]. The spectral response functions (SRFs) of these AHI bands have wavelengths that are slightly longer than those of MODIS bands, as pointed out by Liang et al. [12]. For example, band 7 of AHI has a central wavelength of 3.85 μm , which is longer than that of the MODIS band 20 (3.75 μm for both Aqua and Terra). The same applies to the comparison of (AHI-MODIS) 8.60–8.55, 11.2–11.03, and 12.35–12.02 μm . The comparison between AHI and MODIS has also been conducted to attain spectrally unified and radiometrically consistent observations from these two sensors [13].

The split window algorithm (SWA) is an algorithm that is based on applying the thresholds on two-dimension scatter plots of brightness temperature (BT) and BT difference (BTD). This approach has widely been used for object or cloud classification from space due to its simplicity during this process when compared with other approaches using image segmentation [14], texture analysis [15], and support vector machine [16]. However, these sophisticated methods generally rely on high-speed hardware resources to deal with large datasets [17]. Thus, only a limited number of cloud types can be detected while using machine learning [16]. Another study used the artificial neural network [18], though the analysis was limited to a specific season over a specific region because of the lack of training samples. In contrast, SWA is a simple approach that enables pixel-based cloud classification by only employing limited combinations of a few infrared bands without resorting to the prior processing of segmentation, which is indispensable for most object-based techniques. In this context, SWA is quite suitable for Himawari-8 AHI data that are characterized by a very high temporal resolution and, hence, a considerable volume of data to be processed.

Inoue [19] introduced the first SWA to classify four major types of cloud over the tropical ocean while using the data from NOAA7. Subsequently, SWA was applied to classify six types of cloud [20] based on the cloud height and optical thickness diagram, using the data from NOAA9 [21]. Lutz et al. [22] updated Inoue's SWA method approach to discern seven cloud types while using the same spectral pair (11–12 μm), but combining Meteosat and MODIS data. Hamada et al. [23] further modified the SWA by using millimeter-wave radar and GM-5 data. More recently, Purbantoro et al. [24] applied SWA to the Himawari-8 AHI data. They tested the band combinations of band 13 and 15 (SWA13-15), and band 15 and 16 (SWA15-16), and concluded that, generally, SWA13-15 can detect more cloud types than SWA15-16, though the latter is more sensitive to rain-band clouds such as cumulonimbus. The Japan Meteorological Agency (JMA) developed a cloud masking product of Himawari-8 AHI data, which incorporates discriminations of cloud phase, type, and cloud-top altitude [25]. Additionally, Yamamoto et al. [26] built a cloud detection method, which the JMA cloud mask product verified. The remaining problem with these previous researches is that the use of a visible band is indispensable for constructing the cloud mask [25–30] and, hence, the analysis has so far been limited to the daytime data. Nighttime cloud masks, on the other hand, have been provided in the MODIS standard product

(MYD35/MOD35) [5,31] as well as in other studies, including the polar region [31–34], although all of these studies did not yield products with high temporal coverage, as seen in Himawari-8 AHI. Recently, Lai et al. [29] reported on the study of cloud properties while using the data from AHI, FengYun-4A, and MODIS, but they only treated daytime images. In this context, it is desirable to introduce a method that enables both daytime and nighttime cloud detection while using the very high temporal data of Himawari-8. Besides, the pixel-wise analysis is feasible in a nearly real-time manner since SWA is a simple and mature algorithm [22], even for AHI with a very high data rate. Thus, the aims of the present study are twofold, given the important influence of precise cloud type classification. First, we apply SWA to the images of Himawari-8 AHI, and Aqua or Terra MODIS that are collocated both spatially and temporally. As AHI bands have wavelengths that are slightly longer than those of MODIS bands [12], the comparison is also useful for evaluating the spectral and radiometric capabilities of both sensors in cloud detection and cloud type classification. Second, we propose that the cloud masking process can be applied to both daytime and nighttime data of AHI and MODIS. In this regard, this work is an extension of our previous study [24], in which cloud masking was only discussed for the daytime data of AHI. We employ the Cloud-Aerosol Lidar and Infrared Pathfinder Satellite Observation (CALIPSO) data to validate the present results [35,36], as in our previous case [24]. Additionally, the MODIS standard product (MYD35) [5,31] is exploited to check the probability of detection (POD).

This paper is organized, as follows. In Section 2, we describe the methodology, including the band selection, formulas, and the validation method. Section 3 describes the results, emphasizing the comparison of SWA between Himawari-8 AHI and Aqua/Terra MODIS in cloud type detection. A discussion follows in Section 4, which includes the consideration of validation of the present results. Section 5 will provide the conclusion.

2. Methods

Two nested areas are chosen around Japan as the region of interest (ROI). Figure 1 shows ROI-1 and 2 as BT images from Aqua MODIS and Himawari-8 AHI data. A statistical comparison between MODIS and Himawari-8 data is made using the smaller ROI (ROI-1, 33.1–41.95°N, and 130.06–144.68°E) since MODIS images have a limited swath width of ~2000 km. This choice of a smaller ROI is also advantageous from the viewpoint of the less frequent acquisition of MODIS data. ROI-1 is used for comparing the histograms, scatter diagrams, and choosing threshold values for both MODIS and Himawari-8. However, it is noted that ROI-1 is too small to monitor the temporal changes in cloud types and positions on the synoptic scale and, hence, we define ROI-2 (22.02–47.74°N and 120.11–156.99°E), which covers Japan, South, and North Korea, as well as some parts of China and Russia. For infrared bands, the pixel size of Himawari-8 (0.02 degree) is twice as large as that of MODIS. Nevertheless, we retain their original pixel sizes during the cloud masking and classification analyses, since resizing the pixel size will typically lead to changes in digital numbers.

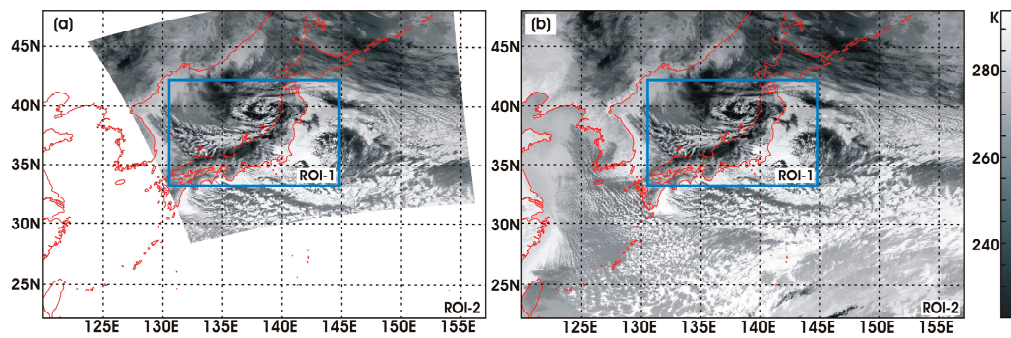


Figure 1. Regional coverage of region of interest (ROI)-1 and ROI-2, shown as brightness temperature (BT) images of (a) Moderate Resolution Imaging Spectroradiometer (MODIS) band 31 and (b) Advanced Himawari Imager (AHI) band 13 observed at 03:40 UTC on February 11, 2017. ROI-1 is used for the statistical comparison, while ROI-2 for cloud identification and classification.

The datasets that are listed in Table 1 are used for the comparison of cloud classification for two seasons (summer and winter) between MODIS and AHI. Subsequently, we employ the CALIPSO data obtained from NASA Langley Research Center to verify the result of cloud classification (<https://www-CALIPSO.larc.nasa.gov/>). The verification is only made for Aqua MODIS data, since no CALIPSO overpass coincidentally occurs with the Terra observation. Moreover, cloud image movies (hereafter AHI cloud movies) with ten-minute intervals are employed using band 4 (0.86 μm) and band 7 (3.9 μm) of Himawari-8 AHI data during the visual interpretation of cloud types and the decision of threshold values.

Table 1. Date and time of the Moderate Resolution Imaging Spectroradiometer (MODIS), Advanced Himawari Imager (AHI), and Cloud-Aerosol Lidar and Infrared Pathfinder Satellite Observation (CALIPSO) datasets. Japan standard time (JST) is + 9 h from UTC.

#Dataset	Date	Aqua/Terra MODIS	Himawari-8 AHI	CALIPSO	Season (Day/Night)
1	10 January 2017	Aqua: 03.40 UTC	03.40 UTC	03.41–03.53 UTC	Winter (Day)
2	11 February, 2017	Aqua: 03.40 UTC	03.40 UTC	03.30–03.44 UTC	Winter (Day)
3	23 January 2017	Terra: 01.30 UTC	01.30 UTC	no overpass data	Winter (Day)
4	24 February 2017	Terra: 01.30 UTC	01.30 UTC	no overpass data	Winter (Day)
5	18 January 2017	Aqua: 16.30 UTC	16.30 UTC	16.29–16.42 UTC	Winter (Night)
6	08 July 2017	Aqua: 04.10 UTC	04.10 UTC	04.11–04.25 UTC	Summer (Day)
7	06 August 2017	Aqua: 03.40 UTC	03.40 UTC	03.39–03.52 UTC	Summer (Day)
8	18 July 2017	Terra: 01.30 UTC	01.30 UTC	no overpass data	Summer (Day)
9	03 August 2017	Terra: 01.30 UTC	01.30 UTC	no overpass data	Summer (Day)
10	14 August 2017	Aqua: 16.30 UTC	16.30 UTC	16.25–16.39 UTC	Summer (Night)

2.1. Band Selection

In this study, the MODIS and AHI data are both acquired from the archive of the Center for Environmental Remote Sensing (CEReS), Chiba University (<http://www.cr.chiba-u.jp/~{}database-jp>). The level of MODIS data is 1B, provided after radiation calibration and geo-correction [37], while AHI data are in the gridded format processed by CEReS. Below, we explain the band selection methods in the cloud classification procedure.

First, cloud masking is carried out for daytime and nighttime data. For daytime, band 3 (R3: here R indicates the band requires the reflection of solar radiation) of MODIS and band 1 (R1) of Himawari-8 AHI are chosen for the albedo calculations. We resize the pixel resolution of a visible band of MODIS and AHI to 1 and 2 km, respectively, in the process of cloud type classification. The images recorded between 09.00–15.00 JST are employed in the daytime dataset. For nighttime cloud masking, on the other hand, we exploit the combinations of several bands, as summarized in Table 2. In this table, for example, R1 represents AHI band 1 reflectance; BT7 represents the brightness temperature of AHI band 7; and, BT31-33 represents the BTD between band 31 and 33 of Aqua MODIS. The Himawari-8

AHI bands employed in cloud masking are bands 1, 7, 12, 13, and 16. Similarly, the MODIS bands 3, 22, 30, 31, and 33 of both Aqua and Terra are employed. The detailed derivation process of these threshold values will be discussed below. The observed images between 20.00–03.00 JST are treated in the nighttime dataset. Table 3 summarizes the central wavelengths and pixel sizes of these bands.

Table 2. Cloud masking method. The method employed for the determination of threshold values is explained in Section 2.5. The central wavelengths of the AHI and MODIS bands are summarized in Table 3. R_x , BT_x , and BT difference $x-y$ (BTD_{x-y}) indicate the reflectance of band x , brightness temperature of band x , and brightness temperature difference between band x and y , respectively.

1. Daytime Cloud Masking			
		Clear Area	Cloudy Area
Himawari-8	Summer and winter	$R_1 < 0.2$	$R_1 \geq 0.2$
Aqua/Terra MODIS	Summer and winter	$R_3 < 0.12$	$R_3 \geq 0.12$
2. Nighttime cloud masking			
Himawari-8 AHI	Land Area	$BT_{13} \geq 256$ K and $BTD_{13-16} \geq 8.2$ K	Otherwise
Winter	Sea Area	$BT_7 \geq 270$ K and $BTD_{7-13} \leq 0.3$ K	Otherwise
Himawari-8 AHI	Land Area	$BT_7 \geq 275$ K and $BT_{7-12} \geq 23.2$ K	Otherwise
Summer	Sea Area	$BT_7 \geq 284$ K and $BTD_{7-13} \leq 4.4$ K	Otherwise
Aqua MODIS	Land Area	$BT_{31} \geq 258$ K and $BTD_{31-33} \geq 11.5$ K	Otherwise
Winter	Sea Area	$BT_{22} \geq 271$ K and $BTD_{22-31} \leq 1.5$ K	Otherwise
Aqua MODIS	Land Area	$BT_{22} \geq 286$ K and $BTD_{22-30} \geq 5.8$ K	Otherwise
Summer	Sea Area	$BT_{22} \geq 271$ K and $BTD_{22-31} \leq 1.5$ K	Otherwise

Table 3. Comparison of bands between Himawari-8 AHI and MODIS. These bands are used for daytime and nighttime cloud mask and classifications.

		AHI (Himawari-8)			MODIS (Aqua/Terra)		
	#Band	Central Wavelength (m)	Pixel Size (km)	#Band	Central Wavelength (m)	Pixel Size (km)	
Visible	1	0.47	1	3	0.469	0.5	
	7	3.9	2	22	3.96	1	
	12	9.6	2	30	9.73	1	
Infrared	13	10.4	2	–	–	–	
	14	11.2	2	31	11.03	1	
	15	12.4	2	32	12.02	1	
	16	13.3	2	33	13.335	1	

Second, we apply the SWA to the band combination of band 13 and 15 for Himawari-8 AHI, and bands 31 and 32 for Aqua/Terra MODIS. As seen from Table 3, all these bands are inside or near the atmospheric window, though the wavelength spacing of the pair is wider for Himawari-8 ($\sim 2 \mu\text{m}$) than for MODIS ($\sim 1 \mu\text{m}$).

Hereafter, for simplicity, “MODIS” refers to both Aqua and Terra MODIS data unless otherwise specified. The observation time of each dataset is indicated while using UTC, which is 9 h behind the Japan standard time (JST).

Figure 2 shows a comparison of histograms between Aqua MODIS and Himawari-8 AHI for visible bands (Figure 2a) and infrared bands (Figure 2b). Similar curves have been obtained from the comparison between the AHI and MODIS results although these histograms are derived from a particular case observed at 03:40 UTC on January 10, 2017. Therefore, they are considered to form the basis of cloud masking and cloud type classification. In Figure 2a, band 3 of Aqua shows a lower albedo value than band 1 of AHI. Overall, the MODIS histograms are closer to each other than those on AHI. Such a feature is ascribable to the fact that bands 1, 2, and 3 of MODIS have more similarity in their visualized images than their counterparts in AHI. Band 3 of AHI exhibits better capability of land detection than band 1 and 2. Moreover, band 1 of AHI can separate cloudy pixels more than bands 2 and 3.

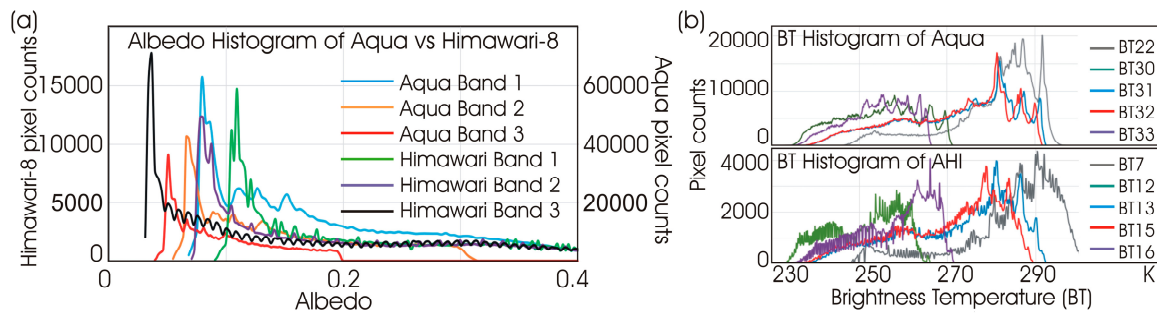


Figure 2. (a) Comparison of albedo histograms of Aqua MODIS versus Himawari-8AHI. (b) Comparison of BT histograms of Aqua MODIS versus Himawari-8 AHI. Both histograms are derived from the images covering ROI-1 acquired at 03.40 UTC on January 10, 2017. The number of AHI pixels is a quarter of MODIS pixels, because of the lower spatial resolution of AHI IR bands (2 km) compared with that of MODIS (1 km).

Figure 2b shows that the BT histograms of Aqua and AHI exhibit a similar trend. Slightly different behavior is found in AHI BT7, in that it exhibits the largest value of the average temperature. It is also larger than that of Aqua BT 22, which has a similar central wavelength to AHI BT7. Aqua BT31 and 32, which are used for SWA31-32, show mostly similar histograms. Although the value of BT31-32 sometimes exhibits negative values, the values of AHI BT13-15 are always positive, since their histograms are separated, as seen in Figure 2b. Such a difference leads to a broader spread of the scatter plot in AHI than in Terra, as explained later in Section 3.2.

2.2. Cloud Masking

Daytime cloud masking is implemented for all of the datasets covering ROI-2 by setting the threshold values of 0.12 for MODIS band 3, and 0.2 for AHI band 1. For this purpose, the albedo of MODIS, A , at the top of the atmosphere (TOA), is derived as [38]:

$$A = (\text{radiance scale}) \times (DN - \text{radiance offset}), \quad (1)$$

while the TOA reflectance of AHI (I) is derived as [39]:

$$I = \text{gain} \times DN + \text{constant}, \quad A = c'I. \quad (2)$$

In these equations, DN stands for the digital number of MODIS or Himawari-8 band under consideration; *radiance scale* and *radiance offset* are the values that are obtained from the MODIS header files. A slightly modified formulation of Equation (2) is employed for the derivation of albedo, A , for AHI. The values of gain, constant, and c' are available in Himawari-8 header files.

As summarized in Table 2, one of the novel aspects of the present study is the proposal of a new method for deriving the nighttime cloud mask by applying different sets of BT and BT D thresholds for sea and land areas in winter and summer seasons. As reported by Wylie et al. [40], the sea area and land area exhibit different values of BT in the mid latitude. They reported that the difference in BT between the winter and summer seasons are typically 20 and 6 K, for land area and sea area, respectively [40].

Figure 3 shows the scatter plot diagram of BT and BT D, which was used to derive the nighttime cloud masking for AHI imagery. The method is based on band 7 (3.9 μm) of AHI or band 22 (3.96 μm) of MODIS, in both sea and land areas. We restrict the time range of data acquisition between 20.00 and 03.00 JST since band 7 and band 22 are infrared bands still affected by the solar reflectance. Sea areas exhibit a lower BT than land areas in most of the IR bands. Band 7 of AHI (band 22 of MODIS) shows the greatest BT among the IR bands (Figure 2b) in both seasons. Thus, we tested the cloud mask method while using two-dimensional scatter plot diagrams of BT7 with BT Ds of BT D7-12, BT D7-13,

BTD7-15, and BTD7-16. We found that, over the sea area, the greatest separation between the cloudy and clear areas is obtained by using the plot of BT7 versus BTD7-13. Over the land area, cloud areas are generally distinguished by using BT7 versus BTD7-12. In the winter season, additional consideration is required for cloud masking over the land area, since snow-covered areas tend to be detected as water clouds. We used BT and BTD based on band 13 and 16 for Himawari-8 in order to cope with this problem; in the case of Aqua, we used band 22 and 33. These band combinations have been chosen based on experimental trials. The pertinent values of thresholds are determined from the visual inspection of datasets, not being limited to the dataset explicitly described in this paper.

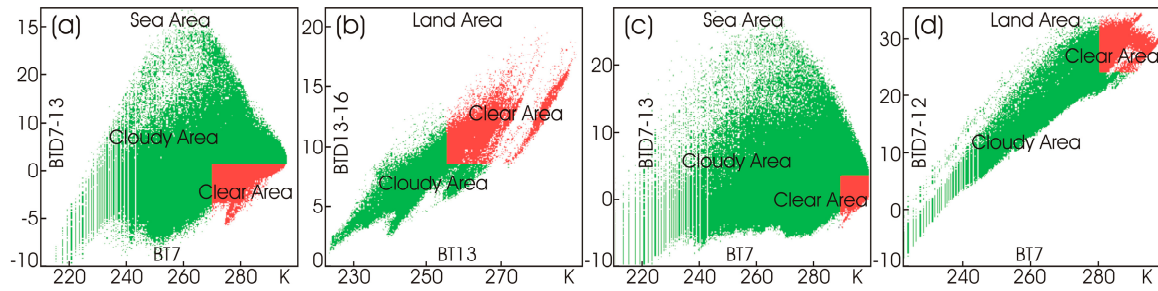


Figure 3. Nighttime cloud masking method using the two-dimensional scatter plot diagram of BT and BTD in winter (a,b) and summer season (c,d) using Himawari-8 AHI data (dataset 5 and 10, respectively). The two datasets are separated into two areas, namely the sea area (a,c) and land area (b,d). Red and green colors indicate the clear and cloud areas, respectively. The threshold values, as determined through the procedure described in Section 2.5, are summarized in Table 2.

2.3. Cloud Classification

During the visual inspection, we also use the AHI cloud movie of band 7 with a ten-minute interval. MODIS standard product (MYD35), as provided by NASA MODIS Adaptive Processing System, Goddard Space Flight Center, USA, validated the results. The BT of MODIS is given by the effective temperature, T_e , being defined as [38]

$$T_e = \frac{hc}{k\lambda} \left[\ln \left(\frac{2hc^2}{\lambda^5 A} + 1 \right) \right]^{-1} \quad (3)$$

Here, h is the Planck constant, k is the Boltzmann constant, and c is the speed of light. The BT of Himawari-8, on the other hand, is calculated by correcting T_e while using constant c_0 , c_1 , and c_2 , which are obtained from Himawari-8 header information files, as [39]

$$BT_{Himawari} = c_0 + c_1 T_e + c_2 T_e^2. \quad (4)$$

We define the following POD for expressing the accuracy of the nighttime cloud mask verified against the MODIS standard product (MYD35/MOD35):

$$POD_{MYD35/MOD35} = \frac{\sum PN_{equal}}{\sum PN_{total}}. \quad (5)$$

Here, PN_{equal} is the number of cloudy or clear pixels determined for Himawari-8/Aqua images that are in agreement with the results that are given in the MYD35/MOD35 cloud mask. The calculation of POD requires identical pixel size and image size, as well as the same gridded geo-location among all of the cloud masks. The verified cloud masks are subsequently used for cloud classification analysis.

The cloud classification is implemented with the SWA while using BT31 and BTD31-32 for MODIS data and BT13 and BTD13-15 for Himawari-8 AHI data within the cloud mask area [24]. Figure 4a shows the matrix of SWA, which has nine regions that represent different cloud types. The regions are separated by the threshold values of BT-1, BT-2, BTD-1, and BTD-2, as listed in Table 4 [24]. These

thresholds have been determined from the visual inspection of a number of datasets, not being limited to the currently described datasets, including images and the AHI cloud movie within the ROI-2 coverage. The type discrimination of clouds is made from their appearance and movement [24].

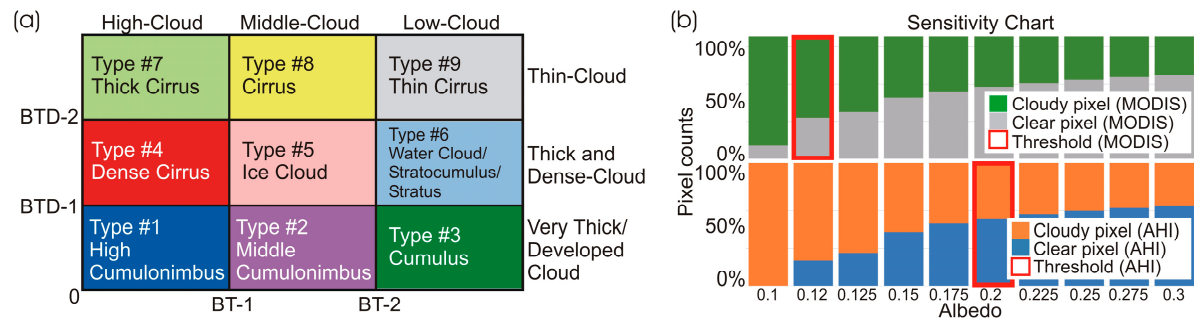


Figure 4. (a) Split window algorithm (SWA) matrix employed for the cloud classification using BT and BT-D values [24]. The nine regions represent nine different types of cloud separated by the threshold values that are listed in Table 4. The same color set is used also in cloud type classification maps to indicate different cloud types. (b) Sensitivity chart used for the determination of albedo thresholds based on band 3 of MODIS and band 1 of Himawari-8 AHI within ROI-1. The threshold values are 0.12 and 0.2 for MODIS and AHI (red boxes), respectively.

Table 4. Threshold values (K) determined for SWA31-32 and SWA13-15 [24].

	Aqua (SWA31-32)		Terra (SWA31-32)		Himawari-8 (SWA13-15)	
Season	winter	summer	winter	summer	winter	summer
BT-1	245	249	242	246	245	250
BT-2	254	257	250	253	253	258
BT-D-1	0.0	0.0	0.0	0.0	0.6	0.9
BT-D-2	2.1	1.7	2.1	1.7	3.2	4.5

2.4. Validation

In this study, the cloud classification results are verified while using CALIPSO data [41,42]. The cloud phase is directly obtained from the depolarization ratio, ρ , of CALIPSO level 2 cloud layer and product data produced at 1 km horizontal resolution. Water cloud (including cumulus) has ρ below 0.1, while the ice cloud (including the cirrus cloud family) has ρ value of more than 0.3 [41–43]. There is a mixed cloud phase with ρ between 0.1 and 0.3, including water cloud, cumulus, and thin cirrus. We define the following POD for evaluating the results in the CALIPSO verification:

$$POD_{Calipso} = \frac{\sum_{i=1}^n P_i}{n}, \tag{6}$$

where the value of P_i is calculated as

$$P_i = \begin{cases} 1, \rho \leq 0 \text{ and CT} = \{\text{Clear area}\}; \\ 0 < \rho \leq 0.1 \text{ and CT} = \{\text{Cu, WC}\}; \\ 0.1 \rightarrow \rho \leq 0.3 \text{ and CT} = \{\text{Cu, WC, IC, DCi, Thick - Ci, Ci, Thin - Ci}\}; \\ \rho \geq 0.3 \text{ and CT} = \{\text{Hi - Cb, Mid - Cb, DCi, IC, Thick - Ci, Ci, Thin - Ci}\}. \\ 0, \text{Otherwise.} \end{cases} \tag{7}$$

and n is the total number of depolarization ratio records within each dataset’s area of coverage ($n = 2010$ for Aqua and 2886 for Himawari-8). CT denotes the cloud type, including Ci: cirrus; DCi: dense cirrus; Thick-Ci: thick cirrus; Thin-Ci: thin cirrus; IC: ice cloud; WC: Water cloud; Hi-Cb: high cumulonimbus; Mid-Cb: middle cumulonimbus; and, Cu: cumulus.

2.5. Determination of Thresholds

The determination of thresholds has been carried out by examining the five datasets that were chosen for each season (summer and winter), excluding those listed in Table 1. The threshold values that are listed in Tables 2 and 4 have been determined by visually inspecting the AHI cloud movie in comparison with the MODIS standard product (MOD35/MYD35) and CALIPSO data, while changing the threshold. The visual discrimination procedure of different cloud types was described in our previous paper [24]. Briefly, we analyzed a total of 40 scenes throughout the year 2016, as well as 30 image movies for each dataset used, equivalent to five-hour records of cloud movements during the AHI visual observation.

Figure 4b shows an example of the sensitivity chart, in which fractions of cloudy and non-cloudy pixels are plotted against the albedo (threshold). This example is for ROI-1 while using Terra/MODIS and AHI data observed at 01.30 UTC on August 3, 2017. The optimal values of the cloud mask thresholds are determined from the condition that the POD using MOD35/MYD35 cloud mask (Equation (5)) is maximized. Similarly, in the case of BT and BTd thresholds in SWA, we calculate the POD while using the depolarization ratio of CALIPSO data (Equations (6) and (7)).

3. Results

3.1. Cloud Mask

Daytime cloud masks of ten datasets (Table 1) are examined within ROI-2 while using Equation (1) for Aqua/Terra MODIS, and Equation (2) for Himawari-8 AHI data. Figure 5 shows the result of cloud masking while using dataset #1, acquired at 03.40 UTC on 10 January 2017. Threshold values for albedo 0.12 and 0.2 have been applied to MODIS and AHI, respectively. As seen in Figure 5a, the value of a MODIS albedo sometimes leads to slightly inaccurate detection; land areas, especially, are sometimes detected as water clouds or cumulus. Additionally, in winter, snow areas over land are occasionally classified as a cloud for both MODIS and AHI images, although the inspection of the AHI cloud movie reduces the possibility of such misdetection. Apart from these problems, no difference has been found in albedo thresholds for the winter and summer seasons.

The nighttime cloud mask has been processed within ROI-2, while using the method formulated in Table 2. The values of BT and BTd are calculated while using Equations (3) and (4). We have determined the best thresholds through the validation against the MODIS standard product (MYD35) [5,31], as summarized in Table 2. The results are also validated using CALIPSO data, as explained in the next sub-section. Although nighttime Terra data concurrent with CALIPSO are unavailable over the study area, the new cloud masking method that was developed for Aqua can apply to Terra data as well.

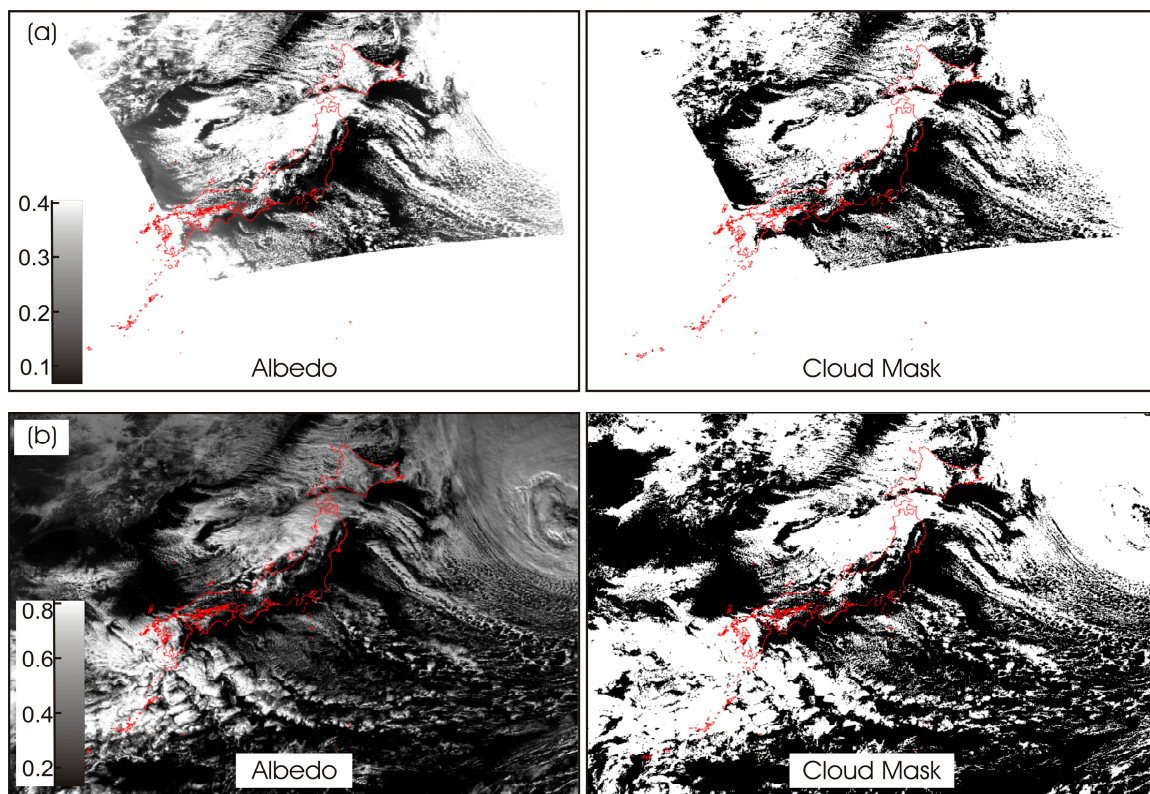


Figure 5. Albedo and daytime cloud mask images derived from dataset #1 acquired at 03.40 UTC on January 10, 2017. (a) Aqua MODIS data and (b) Himawari-8 AHI data. Areas with the highest albedo values, ~ 0.4 for Aqua and ~ 0.8 for Himawari-8, are seen in the Japan Sea area, indicating the presence of a cloud system that often causes heavy snowfall. Pixels with albedo values more than 0.12 (for Aqua) or 0.2 (for Himawari-8) are classified as cloudy. In the cloud mask images, the cloud is indicated with white color, and the clear area with black color.

Figure 6 shows the results of the nighttime cloud mask of Aqua and Himawari-8 datasets (#5 and #10). In comparison with MYD35 cloud mask (b and f), it is found that the new cloud masks (a, c, d, and e) are not as sensitive to very thin water clouds and very thin cirrus clouds as MYD35. Instead, the results that were obtained with new cloud masks appear to be less “noisy”, as seen in regions A and B, for example. This is because very thin clouds tend to exhibit temperatures that are similar to the land or sea surfaces below them and, hence, they are detected as clear areas. Adjusting the threshold values with latitude can alleviate this cloud obscuration effect.

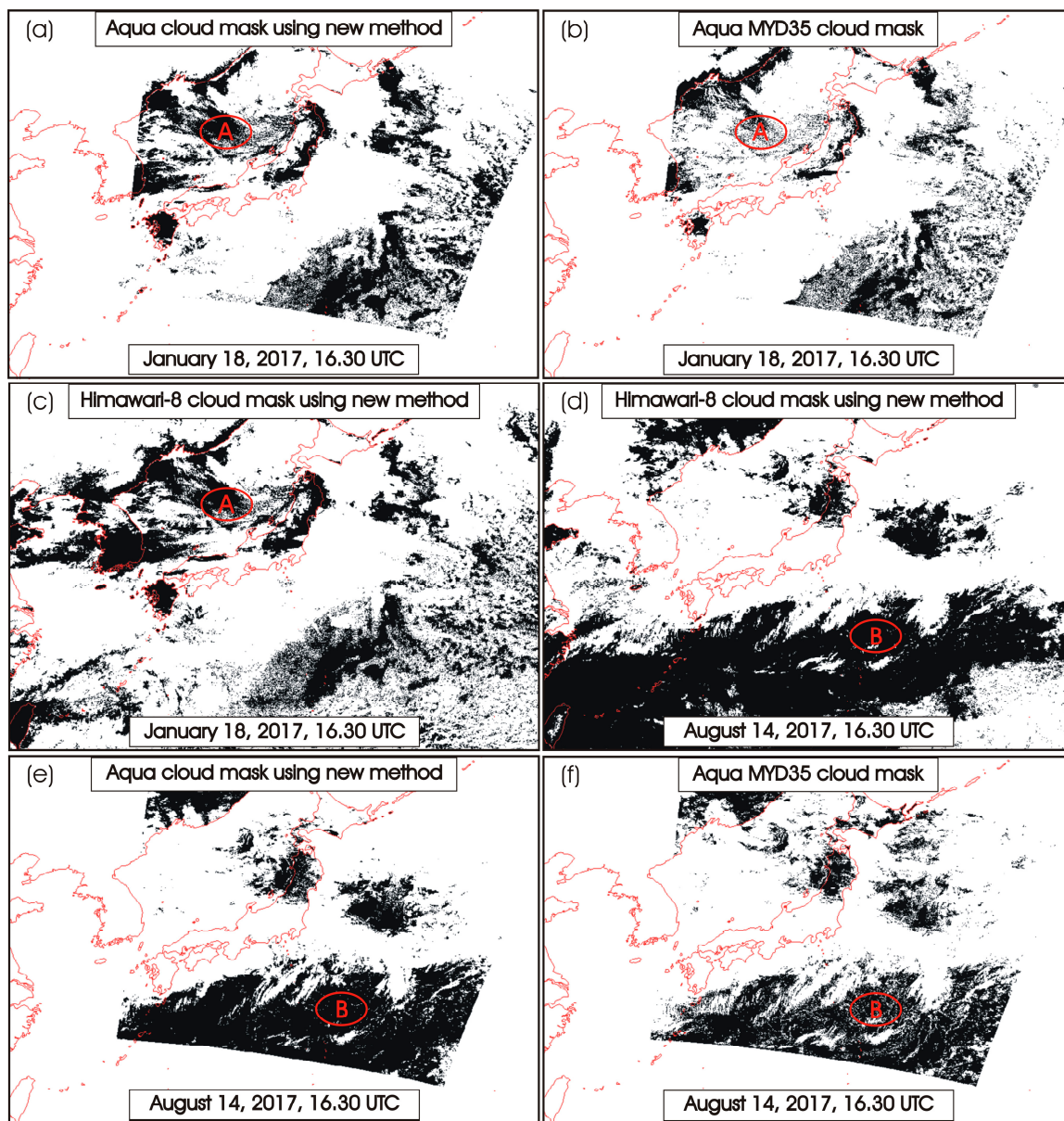


Figure 6. Comparison of nighttime cloud masks within ROI-2, using dataset 5 (a–c) acquired at 16.30 UTC on 18 January 2017, and 10 (d–f) at 16:30 UTC on 14 August 2017. White and black colors represent the cloudy and clear areas, respectively.

3.2. SWA Histograms

The cloud classification using SWA is carried out by constructing the scatter diagram between BT and BT_D. Figure 7 shows the results comparing (a) Aqua, versus (b) Himawari-8, and images acquired at 03.40 UTC on January 10, 2017 (dataset #1), as well as (d) Terra, versus (e) Himawari-8 at 03.40 UTC on August 3, 2017 (dataset #9), both covering ROI-1. The corresponding BT_D histograms are shown in panels (c) and (f). These diagrams have been generated after eliminating the clear area. The cloud type classification of both MODIS and AHI data in daytime and nighttime are derived from nine regions of the scatter plot diagram with the thresholds tabulated in Table 4.

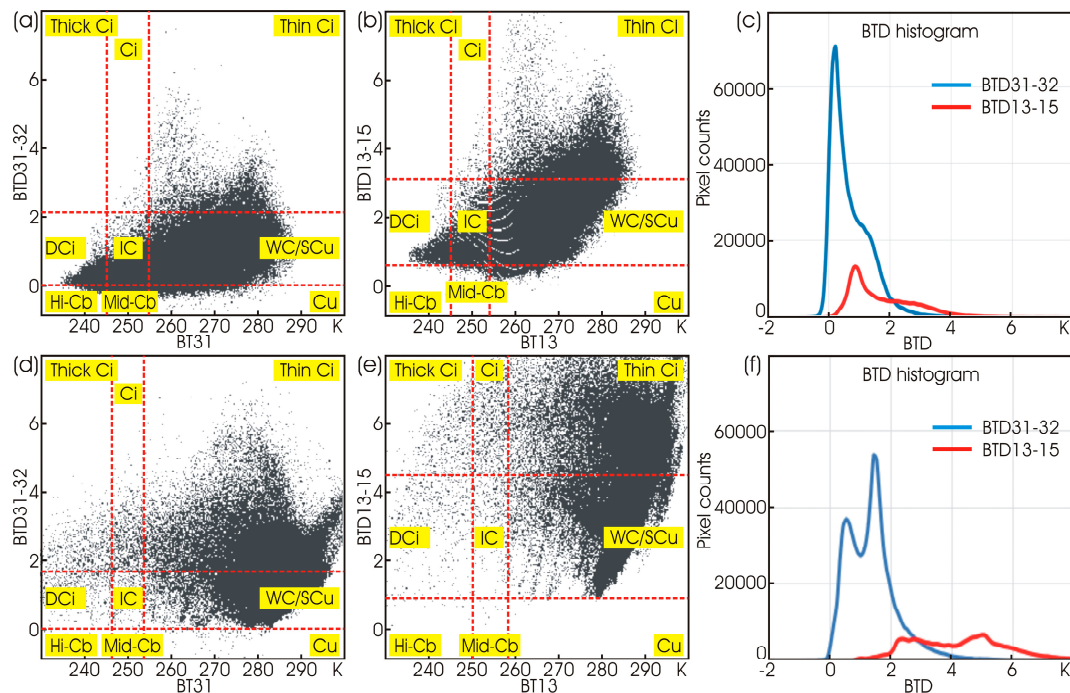


Figure 7. Comparison of scatter plot diagrams of (a) Aqua versus (b) Himawari-8 using dataset #1, and (d) Terra versus (e) Himawari-8 using dataset #9 within ROI-1 coverage. Each show the relationship between BT31 versus BT31–32 for MODIS, or BT13 versus BT13–15 for AHI, consisting of nine regions separated by the thresholds (red lines). The cloud types are indicated with abbreviations of Ci: cirrus, DCi: dense cirrus, IC: ice cloud, WC: Water cloud, SCu: stratocumulus, Hi-Cb: high cumulonimbus, Mid-Cb: middle cumulonimbus, and Cu: cumulus. Panels (c,f) show the BTD histograms of Aqua versus Himawari-8 and Terra versus Himawari-8, respectively. The number of MODIS pixels is four times larger than Himawari-8 pixels.

Generally, the band pair of 31–32 for MODIS, and that of 13–15 for Himawari-8, yield a wider spread of scatter diagram when compared with other choices of infrared band pairs [24]. The resulting scatter plot of Himawari-8 AHI is broader than that of Aqua/Terra MODIS, not being limited to this current dataset. This suggests that there is a possibility of detecting more cloud types with AHI than with MODIS. The inspection of scatter diagrams also indicates the difficulty of discriminating water cloud (WC) and thin cirrus (Ci) though more precisely applying the water vapor band could separate both cloud types. Sometimes dense cirrus and high cumulonimbus (Hi-Cu) are mixed up, especially in the case of a large-scale typhoon or cyclone, although both these types consist of ice clouds at least at the cloud top.

Water cloud (WC)/stratocumulus (Scu) are the most prominent cloud types in Figure 7a,b (dataset 1). Similarly water cloud and thin cirrus dominate Figure 7d,e (dataset 9). Figure 7c,f shows the comparison of BTD histograms of MODIS and AHI. The number of MODIS pixels is four times larger than that of AHI pixels since the pixel size of MODIS (AHI) is 0.01 (0.02) degrees. Moreover, the accumulated number of cloud pixels is different between MODIS and AHI. For example, in the case of dataset 1, the fraction of cloud pixels is 54% for Aqua and 47% for AHI within ROI-1. In the case of dataset 9, it is 60% for Terra and 54% for AHI. The diagrams of Aqua and Terra exhibit negative values of BTD for opaque clouds, while the BTD values of Himawari-8 are always positive, as manifested in the BTD histogram (Figure 7c,f).

3.3. Spatial Distribution of Cloud Types

Figure 8 shows the results of cloud classification, built by combining the result of cloud masking (both daytime and nighttime) and SWA implementation within ROI-2. Figure 8a,b compare the daytime

results of Aqua and Himawari-8 observed in January (dataset 1). The color indication is the same as that shown in Figure 4a. Although no significant differences are found, Aqua MODIS tends to detect slightly more water cloud (light blue) than Himawari-8 AHI. In winter, snow areas, such as those that are seen in the top left part of the coverage area, and some parts of Japan (e.g., Hokkaido Island), are mostly detected as water cloud regions, but they are occasionally detected as cumulus by Aqua (e.g., green color at the top left part of Figure 8a).

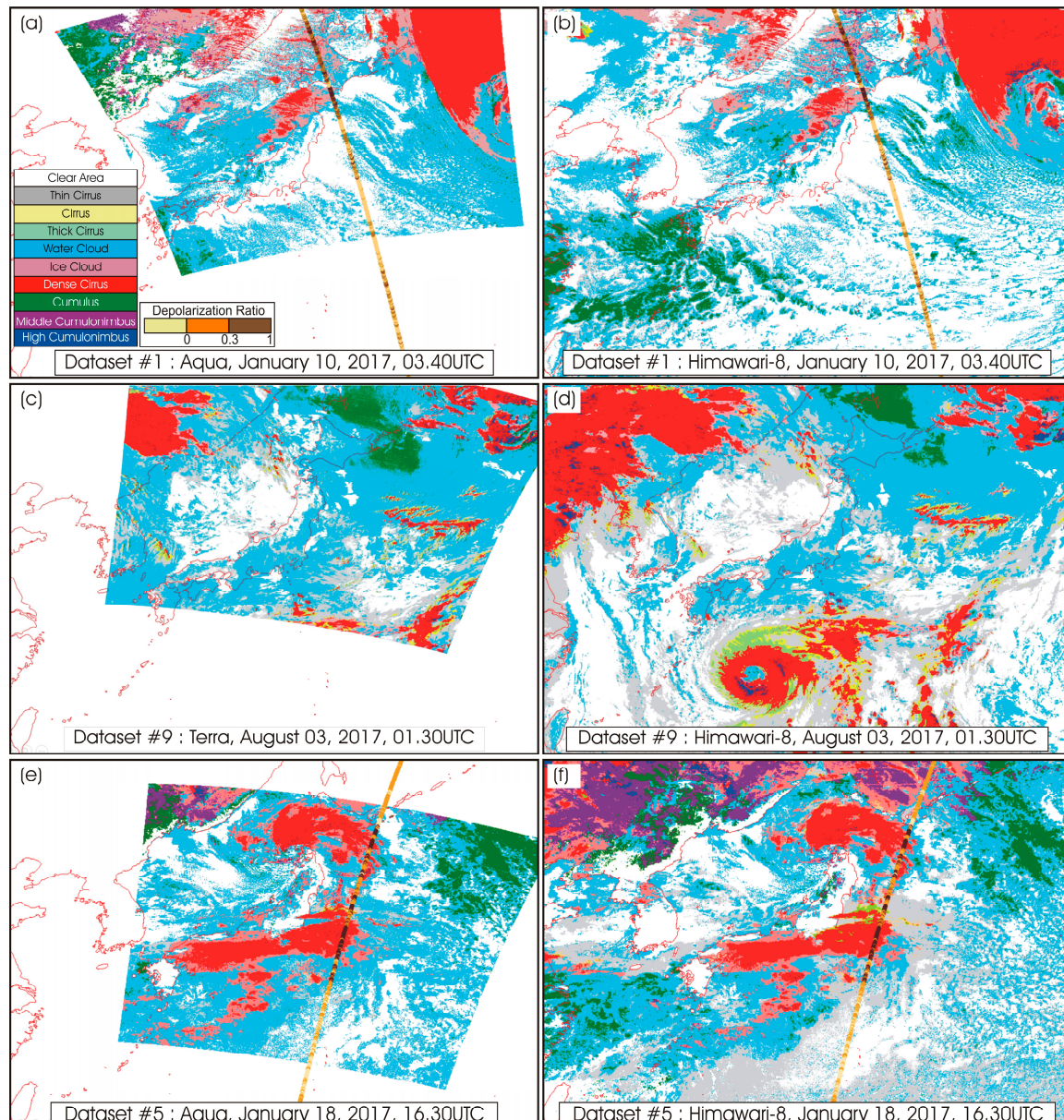


Figure 8. Results of cloud-type classification using the daytime (a–d) and nighttime (e,f) cloud mask. Different colors correspond to those explained in Figure 4, while white color indicates clear areas. The concurrent CALIPSO data are plotted for (a,b) (dataset 1), as well as (e,f) (dataset 5), with colors of the line track of yellow (no depolarization), light brown (water cloud), and dark brown (ice cloud).

Figure 8c,d show the comparison of daytime cloud distributions between the Terra and Himawari-8 images that were observed in summer. A cloud system that is associated with a typhoon is seen on the lower part of the figures. Similarly to Aqua MODIS, Terra MODIS tends to detect slightly more water cloud than Himawari-8 AHI. Sometimes, semi-transparent clouds, such as thin cirrus (grey), are detected as water cloud, because of similar BT.

Figure 8e,f show the results of the nighttime cloud classification (dataset 5). As there is no CALIPSO overpass data concurrent with the Terra MODIS observation in the nighttime, we employ the Aqua MODIS data for this purpose. As a whole, both of the figures show a similarity to the daytime results. By using visual inspection using the AHI cloud movie, thin cirrus (grey) can be recognized over the eastern ocean area, as seen in Figure 8f, though Aqua MODIS detects it as water cloud (light blue). Snow-covered land areas are seen on the top left part of the coverage area (Figure 8f), which are recognized as water cloud and cumulonimbus cloud (purple).

Here, the results of cloud type classification in daytime and nighttime are validated by CALIPSO data by using the depolarization ratio (ρ). More detailed validation processes, while using CALIPSO data, can be found in our previous study [24]. Figure 8 shows the validation result, using three different colors of yellow, light brown, and dark brown, corresponding to $\rho \leq 0$ (no depolarization; clear area), $0 < \rho < 0.3$ (water cloud), and $0.3 \leq \rho$ (ice cloud), respectively. There can be a mixture of water and ice cloud if the value of ρ is between 0.1 and 0.3 [36,41,42]. The CALIPSO categorization of cloud types mostly matches those of MODIS and AHI, as seen from Figure 8. The cloud types of cumulonimbus (dark blue and purple), cirrus (red, light green, yellow, and grey) and ice cloud (pink) correspond to the dark brown ($0.3 \leq \rho$); cumulus (dark green) and water cloud (light blue) correspond to light brown ($0 < \rho < 0.3$). The mixture type ($0 < \rho < 0.3$) sometimes appears as being in the middle part of Figure 8f.

4. Discussion

4.1. Cloud Mask

For the daytime, threshold values of 0.12 for MODIS and 0.2 for AHI have been applied, to obtain the results that are shown in Figure 5 (dataset 1, acquired at 03.40 UTC on 10 January 2017). Generally, MODIS band 3 and AHI band 1 are both affected by the change in solar zenith angle with latitude in daytime cloud detection. This effect causes a slight bias in the determination of thresholds. The difference in albedo between the top and bottom of ROI-1, as measured in the clear area over the ocean, is around 0.01 for both MODIS and AHI data. Previous researches reported that sun glint has significant influence on the analysis of atmospheric aerosol and cloud [44,45]. In the case of Himawari-8, sun glint caused no significant influence in the Japan region. In contrast, the visible bands of Aqua data were often significantly affected by sun glint, which resulted in considerable errors in the cloud masking. In the bottom left of Figure 5a, for instance, we can see a sun glint area in the Aqua albedo image. The ocean surface is sometimes detected as low cloud on such an occasion, since the reflectance of the sun glint area is nearly the same as, or greater than, cloud reflectance. On average, the increase in albedo due to sun glint effects is around 0.04–0.07 in mid-day, Japan time, with the larger effect being observed in summer. The influence of sun glint is mostly negligible in the Japan area since the Terra MODIS observation is performed around 10:30 local time. As such, other studies have successfully removed the sun glint effects from AHI [46] and MODIS data [44,47].

Figure 6 shows the results of the nighttime cloud mask of Aqua and Himawari-8 datasets in January (5) and August (10). For nighttime cloud detection in the winter (5), snow-covered areas reduce the accuracy of cloud detection, since they often exhibit BTs similar to water clouds [48]. This is indeed also the case for both of the new cloud-mask methods. When Equation (5) is applied to dataset 5 (10), for example, the PODs of the new Aqua and Himawari-8 cloud mask are 86.1% and 82.1% (88.4% and 86.2%), respectively.

Figure 7 shows comparisons of scatter plot diagrams between MODIS and AHI. The accumulated number of cloud pixels is different between Aqua (54%) and AHI (47%); this difference is presumably due to more snow-covered pixels being detected as water clouds by MODIS than by AHI (dataset 1). The capability of thin cirrus detection in the daytime is slightly higher for Terra than AHI. This is exemplified in Figure 7d,e, in that the total percentage of the cloud pixels is 60% for Terra, which is higher than the value of 54% for AHI (dataset #9). This difference is ascribable to the fact that the

MODIS sensor is more affected by sun glint, especially in the summer season, as also indicated in a previous study on the MODIS cloud mask [8,29].

4.2. POD Analysis

Table 5 is the summary of the results for all the datasets, which showed that the PODs of cloud mask (columns 4 and 5) are more than 80% on average. The values for dataset 6 (70.2%) and 9 (78.6%) are less than 80%, because of the error due to the sun glint effect in MODIS. For dataset 6, this effect results in the lower POD of cloud classification (60.3%). Such degradations mostly occur when very thin clouds or water clouds are classified as clear area. Dataset 1 of Himawari-8 exhibits a slightly lower POD of 79.0% for the cloud mask, since the dominant type is water cloud, which is often misclassified as a clear area. The PODs of MODIS are higher than those of AHI, presumably because they use the same satellite data as the MYD35/MOD35 standard product. The lower POD is also caused by the strong winds of a temperate cyclone, as manifested in dataset 1. The present results indicate that the proposed method of cloud masking is reliable for both daytime and nighttime when compared with a similar cloud detection study [49], in which the resulting values of POD are around 80% and 73% for MODIS and AHI, respectively.

Table 5. Values of the probability of detection (POD) for daytime and nighttime cloud masking and cloud classification results of Aqua MODIS and Himawari-8 AHI datasets. Cloud mask is validated against the MYD35/MOD35 standard product and cloud classification against the CALIPSO data.

#Dataset	Date	Time (UTC)	Cloud Mask		Cloud Classification	
			POD MODIS	POD AHI	POD MODIS	POD AHI
1	10 January 2017	03.40	83.8%	79.0%	74.0%	77.2%
2	11 February 2017	03.40	87.3%	83.4%	68.5%	74.5%
3	23 January 2017	01.30	88.4%	85.3%	–	–
4	24 February 2017	01.30	88.1%	83.6%	–	–
5	18 January 2017	16.30	86.1%	82.1%	71.9%	69.0%
6	08 July 2017	04.10	70.2%	89.5%	60.3%	60.2%
7	06 August 2017	03.40	83.6%	85.5%	73.2%	62.6%
8	18 July 2017	01.30	86.7%	81.9%	–	–
9	03 August 2017	01.30	78.6%	81.8%	–	–
10	14 August 2017	16.30	88.4%	86.2%	72.2	75.4

It is noted that the detection of very thin cirrus is difficult for both Terra and Himawari-8, which usually categorize it into clear areas. Yamamoto et al. [26] and Xia et al. [50] also pointed out this difficulty, though the additional use of 1.38 m band of MODIS can be effective for distinguishing cirrus clouds in daytime [50]. Moreover, the detection of snow-covered land areas is always difficult, although such situations rarely occur in the Japan area, except in its northern part in winter. Such imperfection of classification can possibly be alleviated by further adjusting the thresholds, by dividing the ROI into smaller regions according to latitude.

In Figure 8, the CALIPSO categorization based on cloud-top features has shown reasonable agreement with the results from MODIS and AHI. It has been found that pixels along the CALIPSO track show better consistency for DCi, Hi-Cb, and Mid-Cb (ice cloud, opaque, deep convective, and $\rho > 0.3$) than other types of water or mixed clouds. The ρ value exhibits variability when cirrus and water clouds are spatially mixed, as in the case of multi-layer clouds (visually observation). The cloud detection in this study is performed assuming single-layer clouds since the cloud detection method is based on the BT of the cloud top. The treatment of multi-layer clouds requires a more detailed approach, such as the use of radiative transfer simulations proposed by Wang et al. [51,52].

A notable difference is seen between Figure 8e and f, since Aqua tends to detect more water clouds (light blue), while Himawari-8 AHI more thin cirrus clouds (grey). According to CALIPSO, these are mostly detected as cirrus clouds. Presumably, this difference is caused by the overlapping features of physical characteristics between water cloud and thin cirrus cloud, as manifested in the scatter plot diagram (Figure 7a). Further adjustment of the BTD-2 threshold might lead to the retrieval of more

thin cirrus detection, although it will reduce the dense cirrus retrieval and overall POD. A similar tendency was, to some extent, found in the Terra dataset (Figure 8c). It is noted that the sensitivity of CALIPSO is much better than that of MODIS and Himawari-8 AHI as far as the detection of a very high transparent cloud layer is concerned, as inferred from Figure 8a,b. In these figures, clear areas that are detected by MODIS and Himawari-8 AHI are occasionally overlapped by the CALIPSO track indicated as cirrus (dark brown).

Table 5 (columns 6 and 7) summarizes the resulting values of the POD of cloud classification for all the datasets. In the case of dataset 1 (#5), Aqua MODIS and Himawari-8 AHI exhibit values of the POD (calculated against CALIPSO data using Equation (6)) of 74.0% and 77.2% (71.9% and 69.0%), respectively. The reduction of POD can be partly brought about by the temporal difference between the three sensors, though the difference is limited (less than 10 min.). Additionally, in the case of dataset #6, the cloud mask error caused by the sun glint has led to a lower POD of cloud classification. Generally, very strong winds, as well as the widespread of mixed-phase clouds, such as those in dataset 5 (Figure 8e,f), for instance, can lead to values of POD that are significantly smaller than the values that are seen under the conditions of homogeneous clouds (e.g., dataset 1). The lower POD of mixed-phase clouds, as compared to homogeneous clouds, is also found in another study [29].

Finally, it is noted that the accuracy of the MODIS standard product (MYD35/MOD35) itself should be checked against other products [53], and, in this regard, further examination by employing the high-frequency data from Himawari-8 AHI could be meaningful. Besides, it is worth noting that the area in the present analysis is somewhat limited, both spatially (22.02–47.74°N and 120.11–156.99°E) and temporally (09:00–15:00 and 20:00–03:00 JST). In view of the differences in cloud formation mechanisms, the applicability of SWA for other regions should be investigated in future work. Additionally, it is necessary to study how the spatial resolution of satellite sensors can affect the results of cloud detection and cloud classification, since both MODIS and AHI are relatively low-resolution sensors.

5. Conclusions

The comparison between Aqua/Terra MODIS and Himawari-8 AHI for cloud type detection in both the daytime and nighttime has been described, including the proposal of a new method of nighttime cloud masking. The proposed method is based on the difference of the radiance values over the cloudy and clear areas while using several wavelength bands. This leads to the difference in the brightness temperature response over the land and sea areas. The verification of the cloud masking results has been performed against the MODIS standard product (MYD35/MOD35). It has been found that MODIS and AHI both lead to acceptable results in cloud masking, which gives POD values that exceed 80%. Sun glint affects the daytime MODIS cloud masking, especially in summer. This effect leads to the change in the albedo of 0.04–0.07, although the effect is insignificant for Himawari-8 AHI imagery.

Regarding the application of the SWA on MODIS and AHI, the novel aspect of the present study is that the combination of 10 and 12 μm bands is used for Himawari-8 AHI, and that of 11 and 12 μm bands for Aqua/Terra MODIS. From the scatter plot diagram between BT and BT_D, it can be seen that Himawari-8 AHI provides more spread of points in the scatter diagram, which gives the possibility of detecting more cloud types than MODIS. The results of the cloud type classification have been verified by using the depolarization ratio data from the concurrent CALIPSO data, which results in POD values of more than 70% on average. In the future, similar efforts, which exploit the very high temporal resolution data of Himawari-8 and other third-generation meteorological satellites, will provide better opportunities to understand cloud behavior and contribute to climate change studies.

Author Contributions: Conceptualization, B.P., J.T.S.S. and H.K.; methodology, B.P., K.T., N.L., and H.K.; software, B.P., J.A., and N.M.; validation, B.P., N.M., K.T., and H.K.; formal analysis, B.P., N.L., and H.K.; writing—original draft preparation, B.P., and H.K.; writing—review and editing, B.P., and H.K.; supervision, J.T.S.S., and H.K.

Funding: This research received no external funding.

Acknowledgments: One of the authors (B.P.) expresses his gratitude to the financial support of Ministry of Research, Technology and Higher Education (RISTEKDIKTI), Republic of Indonesia, through the Scholarship Program for Research and Innovation in Science and Technology (RISET-Pro).

Conflicts of Interest: The authors declare no conflict of interest.

References

1. Schneider, S.H. Cloudiness as a Global Climatic Feedback Mechanism: The Effects on the Radiation Balance and Surface Temperature of Variations in Cloudiness. *J. Atmos. Sci.* **1972**, *29*, 1413–1422. [[CrossRef](#)]
2. Arking, A.; Childs, J.D. Retrieval of Cloud Cover Parameters from Multispectral Satellite Images. *J. Clim. Appl. Meteorol.* **1985**, *24*, 322–333. [[CrossRef](#)]
3. Li, J.; Menzel, W.P.; Yang, Z.; Frey, R.A.; Ackerman, S.A. High-Spatial-Resolution Surface and Cloud-Type Classification from MODIS Multispectral Band Measurements. *J. Appl. Meteorol.* **2003**, *42*, 204–226. [[CrossRef](#)]
4. Li, J.; Menzel, W.P.; Sun, F.; Schmit, T.J.; Gurka, J. AIRS Subpixel Cloud Characterization Using MODIS Cloud Products. *J. Appl. Meteorol.* **2004**, *43*, 1083–1094. [[CrossRef](#)]
5. Ackerman, S.A.; Strabala, K.I.; Menzel, W.P.; Frey, R.A.; Moeller, C.C.; Gumley, L.E. Discriminating Clear Sky from Clouds with MODIS. *J. Geophys. Res.* **1998**, *103*, 32141–32157. [[CrossRef](#)]
6. Platnick, S.; King, M.D.; Ackerman, S.A.; Menzel, W.P.; Baum, B.A.; Riédi, J.C.; Frey, R.A. The MODIS Cloud Products: Algorithms and Examples from Terra. *IEEE Trans. Geosci. Remote Sens.* **2003**, *41*, 459–473. [[CrossRef](#)]
7. Barnes, W.L.; Pagano, T.S.; Salomonson, V.V. Prelaunch Characteristics of the Moderate Resolution Imaging Spectroradiometer (MODIS) on EOS-AMI. *IEEE Trans. Geosci. Remote Sens.* **1998**, *36*, 1088–1100. [[CrossRef](#)]
8. Frey, R.A.; Ackerman, S.A.; Liu, Y.; Strabala, K.I.; Zhang, H.; Key, J.R.; Wang, X. Cloud Detection with MODIS. Part I: Improvements in the MODIS Cloud Mask for Collection 5. *J. Atmos. Ocean. Technol.* **2008**, *25*, 1057–1072. [[CrossRef](#)]
9. Strabala, K.I.; Ackerman, S.A.; Menzel, W.P. Cloud Properties Inferred from 8–12 μ m Data. *J. Appl. Meteorol. Meteorol.* **1994**, *33*, 212–229. [[CrossRef](#)]
10. Hall, D.K.; Riggs, G.A.; Salomonson, V.V.; DiGirolamo, N.E.; Bayr, K.J. MODIS Snow-Cover Products. *Remote Sens. Environ.* **2002**, *83*, 181–194. [[CrossRef](#)]
11. Bessho, K.; Date, K.; Hayashi, M.; Ikeda, A.; Imai, T.; Inoue, H.; Kumagai, Y.; Miyakawa, T.; Murata, H.; Ohno, T.; et al. An Introduction to Himawari-8/9. *J. Meteorol. Soc. Jpn.* **2016**, *94*, 151–183. [[CrossRef](#)]
12. Liang, X.; Ignatov, A.; Kramar, M.; Yu, F. Preliminary Inter-Comparison between AHI, VIIRS and MODIS Clear-Sky Ocean Radiances for Accurate SST Retrievals. *Remote Sens.* **2016**, *8*, 203. [[CrossRef](#)]
13. Qin, Y.; McVicar, T.R. Spectral Band Unification and Inter-Calibration of Himawari AHI with MODIS and VIIRS: Constructing Virtual Dual-View Remote Sensors from Geostationary and Low-Earth-Orbiting Sensors. *Remote Sens. Environ.* **2018**, *209*, 540–550. [[CrossRef](#)]
14. Yuan, Y.; Hu, X. Bag-of-Words and Object-Based Classification for Cloud Extraction from Satellite Imagery. *IEEE J. Sel. Top. Appl. Earth Obs. Remote Sens.* **2015**, *8*, 4197–4205. [[CrossRef](#)]
15. Christodoulou, C.I.; Michaelides, S.C.; Pattichis, C.S. Multi-feature Texture Analysis for the Classification of Clouds in Satellite Imagery. *IEEE Trans. Geosci. Remote Sens.* **2003**, *41*, 2662–2668. [[CrossRef](#)]
16. Lee, Y.; Wahba, G.; Ackerman, S.A. Cloud Classification of Satellite Radiance Data by Multicategory Support Vector Machines. *J. Atmos. Ocean. Technol.* **2004**, *21*, 159–169. [[CrossRef](#)]
17. Hay, G.J.; Castilla, G. Object-Based Image Analysis: Strengths, Weaknesses, Opportunities and Threats (SWOT). *Int. Arch. Photogramm. Remote Sens. Spat. Inf. Sci.* **2006**, *36*, 4.
18. Liu, Y.; Xia, J.; Shi, C.X.; Hong, Y. An Improved Cloud Classification Algorithm for China's FY-2C Multi-Channel Images Using Artificial Neural Network. *Sensors* **2009**, *9*, 5558–5579. [[CrossRef](#)]
19. Inoue, T. A Cloud Type Classification with NOAA 7 Split-Window Measurements. *J. Geophys. Res.* **1987**, *92*, 3991–4000. [[CrossRef](#)]
20. Inoue, T.; Ackerman, S.A. Radiative Effects of Various Cloud Types as Classified by the Split Window Technique over the Eastern Sub-tropical Pacific Derived from Collocated ERBE and AVHRR Data. *J. Meteorol. Soc. Jpn.* **2002**, *80*, 1383–1394. [[CrossRef](#)]
21. Luo, Z.; Rossow, W.B.; Inoue, T.; Stubenrauch, C.J. Did the Eruption of the Mt. Pinatubo Volcano Affect Cirrus Properties? *J. Clim.* **2002**, *15*, 2806–2820. [[CrossRef](#)]

22. Lutz, H.-J.; Inoue, T.; Schmetz, J. Notes and Correspondence Comparison of a Split-window and a Multi-spectral Cloud Classification for MODIS Observations. *J. Meteorol. Soc. Jpn.* **2003**, *81*, 623–631. [[CrossRef](#)]
23. Hamada, A.; Nishi, N.; Kida, H.; Shiotani, M.; Iwasaki, S.; Kamei, A.; Ohno, Y.; Kuroiwa, H.; Kumagai, H.; Okmoto, H. Cloud type classification by GMS-5 infrared split window measurements with millimeter-wave radar and TRMM observations in the tropics. In Proceedings of the 2nd TRMM International Science Conference, Nara, Japan, 6–10 September 2004.
24. Purbantoro, B.; Aminuddin, J.; Manago, N.; Toyoshima, K.; Lagrosas, N.; Sumantyo, J.T.S.; Kuze, H. Comparison of Cloud Type Classification with Split Window Algorithm Based on Different Infrared Band Combinations of Himawari-8 Satellite. *Adv. Remote Sens.* **2018**, *7*, 218–234. [[CrossRef](#)]
25. Imai, T.; Yoshida, R. Algorithm Theoretical Basis for Himawari-8 Cloud Mask Product. *Meteorol. Satell. Cent. Tech. Note* **2016**, *61*, 1–17. Available online: <https://www.data.jma.go.jp/mscweb/technotes/msctechrep61-1.pdf> (accessed on 20 July 2019).
26. Yamamoto, Y.; Ishikawa, H.; Oku, Y.; Hu, Z. An Algorithm for Land Surface Temperature Retrieval Using Three Thermal Infrared Bands of Himawari-8. *J. Meteorol. Soc. Jpn. Ser. II* **2018**, *96*, 43. [[CrossRef](#)]
27. Kopp, T.J.; Thomas, W.; Heidinger, A.K.; Botambekov, D.; Frey, R.A.; Hutchison, K.D.; Iisager, B.D.; Brueske, K.; Reed, B. The VIIRS Cloud Mask: Progress in the First Year of S-NPP Toward a Common Cloud Detection Scheme. *J. Geophys. Res. Atmos.* **2014**, *119*, 2441–2456. [[CrossRef](#)]
28. Murino, L.; Amato, U.; Carfora, M.F.; Antoniadis, A.; Huang, B.; Menzel, W.P.; Serio, C. Cloud Detection of MODIS Multispectral Images. *J. Atmos. Ocean. Technol.* **2014**, *31*, 347–365. [[CrossRef](#)]
29. Lai, R.; Teng, S.; Yi, B.; Letu, H.; Min, M.; Tang, S.; Liu, C. Comparison of Cloud Properties from Himawari-8 and FengYun-4A Geostationary Satellite Radiometers with MODIS Cloud Retrievals. *Remote Sens.* **2019**, *11*, 1703. [[CrossRef](#)]
30. Shang, H.; Chen, L.; Letu, H.; Zhao, M.; Li, S.; Bao, S. Development of A Daytime Cloud and Haze Detection Algorithm for Himawari-8 Satellite Measurements Over Central and Eastern China. *J. Geophys. Res.* **2017**, *122*, 3528–3543. [[CrossRef](#)]
31. Ackerman, S.A.; Holz, R.E.; Frey, R.; Eloranta, E.W.; Maddux, B.C.; McGill, M. Cloud Detection with MODIS. Part II: Validation. *J. Atmos. Ocean. Technol.* **2008**, *25*, 1073–1086. [[CrossRef](#)]
32. Derrien, M.; Farki, B.; Harang, L.; LeGléau, H.; Noyalet, A.; Pochic, D.; Sairouni, A. Automatic Cloud Detection Applied to NOAA-11/AVHRR Imagery. *Remote Sens. Environ.* **1993**, *46*, 246–267. [[CrossRef](#)]
33. Trepte, Q.; Minnis, P.; Arduini, R.F. Daytime and Nighttime Polar Cloud and Snow Identification Using MODIS Data. *Opt. Remote Sens. Atmos. Clouds III* **2003**, *4891*, 449–459.
34. Liu, Y.; Key, J.R.; Frey, R.A.; Ackerman, S.A.; Menzel, W.P. Nighttime Polar Cloud Detection with MODIS. *Remote Sens. Environ.* **2004**, *92*, 181–194. [[CrossRef](#)]
35. Winker, D.M.; Pelon, J.R.; McCormick, M.P. The CALIPSO Mission: Spaceborne Lidar for Observation of Aerosols and Clouds. *Lidar Remote Sens. Ind. Environ. Monit. III* **2003**, *4893*, 1–11.
36. Hu, Y.; Winker, D.; Vaughan, M.; Lin, B.; Omar, A.; Trepte, C.; Flittner, D.; Yang, P.; Nasiri, S.L.; Baum, B.; et al. CALIPSO/CALIOP Cloud Phase Discrimination Algorithm. *J. Atmos. Ocean. Technol.* **2009**, *26*, 2293–2309. [[CrossRef](#)]
37. Isaacman, A.T.; Toller, G.N.; Barnes, W.L.; Guenther, B.W.; Xiong, X. MODIS Level 1B Calibration and Data Products. In Proceedings of the Optical Science and Technology, SPIE’s 48th Annual Meeting, San Diego, CA, USA, 3–8 August 2003; Volume 5151, pp. 552–562.
38. Toller, G.N.; Isaacman, A.; Leader, M.T.; Salomonson, V. MODIS Level 1B Product User’s Guide. Signature 2003. Available online: https://mcst.gsfc.nasa.gov/sites/default/files/file_attachments/M1054E_PUG_2017_0901V6.2.2_Terra_V6.2.1_Aqua.pdf (accessed on 20 July 2019).
39. Japan Meteorological Agency Himawari-8/9 Standard Data User’s Guide Version 1.2. 2015. Available online: https://www.data.jma.go.jp/mscweb/en/himawari89/space_segment/hsd_sample/HS_D_users_guide_en_v12.pdf (accessed on 20 July 2019).
40. Wylie, D.P.; Menzel, W.P. Eight Years of High Cloud Statistics Using HIRS. *J. Clim.* **1999**, *12*, 170–184. [[CrossRef](#)]
41. Cho, H.-M.; Yang, P.; Kattawar, G.W.; Nasiri, S.L.; Hu, Y.; Minnis, P.; Trepte, C.; Winker, D. Depolarization Ratio and Attenuated Backscatter for Nine Cloud Types: Analyses Based on Collocated CALIPSO Lidar and MODIS Measurements. *J. Geophys. Res. Atmos.* **2008**, *16*, 3931–3948. [[CrossRef](#)]

42. Hu, Y. Depolarization Ratio–Effective Lidar Ratio Relation: Theoretical Basis for Space Lidar Cloud Phase Discrimination. *Geophys. Res. Lett.* **2007**, *34*, 6–9. [[CrossRef](#)]
43. Hu, Y.X.; Yang, P.; Lin, B.; Gibson, G.; Hostetler, C. Discriminating Between Spherical and Non-Spherical Scatterers with Lidar Using Circular Polarization: A Theoretical Study. *J. Quant. Spectrosc. Radiat. Transf.* **2003**, *79*, 757–764. [[CrossRef](#)]
44. Hu, C. An Empirical Approach to Derive MODIS Ocean Color Patterns under Severe Sun Glint. *Geophys. Res. Lett.* **2011**, *38*, 1–5. [[CrossRef](#)]
45. Wang, M.; Bailey, S.W. Correction of Sun Glint Contamination on the Sea WiFS Ocean and Atmosphere Products. *Appl. Opt.* **2001**, *40*, 4790–4798. [[CrossRef](#)] [[PubMed](#)]
46. Lee, S.H.; Kim, B.Y.; Lee, K.T.; Zo, I.S.; Jung, H.S.; Rim, S.H. Retrieval of Reflected Shortwave Radiation at the Top of the Atmosphere Using Himawari-8/AHI Data. *Remote Sens.* **2018**, *10*, 213. [[CrossRef](#)]
47. Zhang, H.; Wang, M. Evaluation of Sun Glint Models Using MODIS Measurements. *J. Quant. Spectrosc. Radiat. Transf.* **2010**, *111*, 492–506. [[CrossRef](#)]
48. Frei, A.; Tedesco, M.; Lee, S.; Foster, J.; Hall, D.K.; Kelly, R.; Robinson, D.A. A Review of Global Satellite-Derived Snow Products. *Adv. Space Res.* **2012**, *50*, 1007–1029. [[CrossRef](#)]
49. Shang, H.; Letu, H.; Nakajima, T.Y.; Wang, Z.; Ma, R.; Wang, T.; Lei, Y.; Ji, D.; Li, S.; Shi, J. Diurnal Cycle and Seasonal Variation of Cloud Cover over the Tibetan Plateau as Determined from Himawari-8 New-Generation Geostationary Satellite Data. *Sci. Rep.* **2018**, *8*, 1105. [[CrossRef](#)]
50. Xia, L.; Zhao, F.; Chen, L.; Zhang, R.; Mao, K.; Kylling, A.; Ma, Y. Performance Comparison of the MODIS and the VIIRS 1.38 μm Cirrus Cloud Channels Using LibRadtran and CALIOP Data. *Remote Sens. Environ.* **2018**, *206*, 363–374. [[CrossRef](#)]
51. Wang, J.; Liu, C.; Min, M.; Hu, X.; Lu, Q.; Husi, L. Effects and Applications of Satellite Radiometer 2.25 μm Channel on Cloud Property Retrievals. *IEEE Trans. Geosci. Remote Sens.* **2018**, *56*, 5207–5216. [[CrossRef](#)]
52. Wang, J.; Liu, C.; Yao, B.; Min, M.; Letu, H.; Yin, Y.; Yung, Y.L. A Multilayer Cloud Detection Algorithm for the Suomi-NPP Visible Infrared Imager Radiometer Suite (VIIRS). *Remote Sens. Environ.* **2019**, *227*, 1–11. [[CrossRef](#)]
53. Wang, T.; Fetzer, E.J.; Wong, S.; Kahn, B.H.; Yue, Q. Validation of MODIS Cloud Mask and Multilayer Flag Using CloudSat-CALIPSO Cloud Profiles and a Cross-Reference of their Cloud Classifications. *J. Geophys. Res. Atmos.* **2016**, *121*, 11620–11635. [[CrossRef](#)]



© 2019 by the authors. Licensee MDPI, Basel, Switzerland. This article is an open access article distributed under the terms and conditions of the Creative Commons Attribution (CC BY) license (<http://creativecommons.org/licenses/by/4.0/>).